



Controllable ZnFe₂O₄/reduced graphene oxide hybrid for high-performance supercapacitor electrode

Shuhua Yang^a, Zhenzhen Han^a, Jing Sun^a, Xiaopeng Yang^a, Xun Hu^a, Cuncheng Li^b, Bingqiang Cao^{a,*}

^a Materials Center for Energy and Photoelectrochemical Conversion, School of Material Science and Engineering, University of Jinan, Jinan 250022, China

^b School of Chemistry and Chemical Engineering, University of Jinan, Jinan 250022, China



ARTICLE INFO

Article history:

Received 23 December 2017

Received in revised form

25 January 2018

Accepted 4 February 2018

Available online 19 February 2018

Keywords:

ZnFe₂O₄

Reduced graphene oxide

Mass ratio

Particle size

Supercapacitor

ABSTRACT

Here, a controllable ZFO/rGO hybrid is prepared with high SCs performance by controlling the ZFO particle size and ZFO mass ratio. Small ZFO nanoparticles (~15 nm) can be fully utilized and facilitated fast ion transport during electrochemical reactions, whereas the high mass ratio of ZFO (82.3%) will improve the specific capacitance of the ZFO/rGO hybrid electrode. The specific capacitance of this hybrid reach 352.9 F g⁻¹ at current densities of 1 A g⁻¹, which is higher or comparable to other ZFO based electrodes. It also exhibits remarkable cyclic stability (92.3% retention after 10000 cycles) and good rate performance. In addition, the energy density of symmetric supercapacitor based on ZFO/rGO hybrid can reach 6.7 Wh kg⁻¹ at a power density of 300 W kg⁻¹ within a voltage of 1.2 V in a 2 M KOH aqueous electrolyte.

© 2018 Elsevier Ltd. All rights reserved.

1. Introduction

With the growing demand for clean energy, supercapacitors (SCs), as a promising energy storage technology, have attracted considerable interest due to their high power density, fast recharge capability, and long cycling life [1–3]. Supercapacitors can be classified into carbon-based electrochemical double layer capacitors (EDLCs) and redox-based pseudocapacitors based on the charge storage mechanisms [4–8]. EDLCs store charges electrostatically and offer a high power density but relatively low energy density. Then much work focused on pseudocapacitive electrode materials such as transition metal oxides (RuO₂, MnO₂, Co₃O₄, NiO) and conducting polymers (polyaniline, polypyrrole and polythiophene), which can increase capacitance via reversible redox reactions [9–16]. Among them, spinel transition metal oxide (AB₂O₄) is emerging due to the unique electronic structures and the utilization of two metal elements [17–19].

ZnFe₂O₄ (ZFO) is one of the most promising spinel transition metal oxide for SCs electrode because of its much better electrical conductivity and higher electrochemical activity [20–22].

However, its electrical conductivity is still not high enough to be kinetically favorable, thereby limiting their use. In recent years, the development of incorporating carbon materials with ZnFe₂O₄ has been considered as an effective approach for achieving high-performance. Vadiyar et al. have investigated ZnFe₂O₄ nanoflake@ZnFe₂O₄/C nanoparticle heterostructure electrode, in which the conductivity is greatly improved by carbon nanoparticles [17]. Graphene with atom-thick layer features, has attracted much attention recently for conductive substrate/scaffold due to its high specific surface area, fast electron transfer ability, and good mechanical properties. The unique characteristics of graphene inspired us to design and synthesize graphene-supported ZFO hybrid. Li et al. have prepared the ZnFe₂O₄/NRG composite, and the ZnFe₂O₄/NRG composite as supercapacitor electrode exhibits a favorable specific capacitance of 244 F g⁻¹ at 0.5 A/g [23]. Although some achievements have been made in ZFO/graphene, there is no study focused on the ZFO mass ratio and the ZFO particle size control in the composites and their influence on SCs performances. Hence, the development of ZFO/graphene hybrid system with high ZFO mass ratio and controllable ZFO particle size in the composites and investigation of its SCs performances is of fundamental and practical significance.

In this work, we report a ZFO/reduced graphene oxide (ZFO/rGO) hybrid with high ZFO mass ratio (82.3%) and average ZFO

* Corresponding author.

E-mail address: mse_caobq@ujn.edu.cn (B. Cao).

diameters of ~15 nm dispersed on the graphene surfaces via a one-step hydrothermal method. Small ZFO nanoparticles can be fully utilized and facilitated fast ion transport during electrochemical reactions, whereas the high mass ratio of ZFO can improve the specific capacitance of the composite electrode. Therefore, the specific capacitances of the ZFO/rGO electrode at current densities of 1 A g^{-1} can reach 352.9 F g^{-1} . Enhanced rate capability and excellently cycling stability (92.3% retention after 10000 cycles) were also observed.

2. Experimental section Section

2.1. Preparation of ZFO/rGO hybrid

All chemicals were of analytical grade in this study and used as received without further purification. Graphite oxide (GO) was synthesized using natural graphite according to the reported method [24]. The ZFO/reduced graphene oxide (ZFO/rGO) hybrid was fabricated by a facile hydrothermal process. In a typical synthesis, $\text{FeCl}_3 \cdot 6\text{H}_2\text{O}$ and ZnCl_2 in the molar ratio 2:1 was dissolved into 30 mL of ethylene glycol by stirring at room temperature. Then 0.54 g of NaAc, 0.5 g of polyethylene glycol (PEG-4000), and 10 mL of homogeneous GO solution (3 mg mL^{-1}) was added to the suspension. NaAc was used as a precipitation agent in the preparation of ZFO nanomaterials. After vigorous agitation for 30 min, the mixture solution was transferred into a 50 mL Teflon-lined stainless steel autoclave and heated at 200°C for 24 h. Then, the as-obtained product was washed with Milli-Q water and ethanol through centrifugation for several times, and then air-drying at 60°C for 24 h. The ZFO/rGO hybrid with different ratios of graphene and ZFO were synthesized and characterized (Table S1 and Fig. S1).

2.2. Characterization

The characterization of the morphologies was analyzed by field emission scanning electron microscopy (SEM, Quanta 250 FEG, FEI) and transmission electron microscopy (TEM, JEM-2010F, JEOL). The crystal structures of ZFO were characterized by powder X-ray diffraction (XRD, D8-Advance, Bruker). Raman spectra were taken on Thermo Scientific Raman Microscope DXR with a 532 nm laser excitation length. The weight ratio of the ZFO nanoparticles was determined by thermogravimetric analysis (TGA) using thermogravimetric analyzer (TGA, TGA/DSC 1/1600HT, Mettler-Toledo) at a heating rate of $10^\circ\text{C min}^{-1}$ in air. The specific surface area were examined by N_2 adsorption-desorption isotherms through an Autosorb-iQ-C-TCD.TRX full-automatic physical and chemical

adsorption analyzer.

2.3. Electrochemical measurements

Electrochemical performance of electrodes was examined by three-electrode system and symmetric supercapacitor in a 2 M KOH aqueous electrolyte on Zahner/Zennium electrochemical workstation. In three-electrode system, a platinum foil ($1 \text{ cm} \times 1 \text{ cm}$) auxiliary electrode and a Ag/AgCl reference electrode was used. The working electrodes were prepared by mixing the active materials, acetylene black, and a polyvinylidene difluoride (PVDF) binder by a mass ratio of 80: 10: 10 in N-methyl pyrrolidone (NMP) solvent. Then the mixed slurry was coated onto the nickel foam substrate ($1 \text{ cm} \times 1 \text{ cm}$) and pressed under the pressure of 10 MPa, followed by drying at 60°C for 24 h to make electrodes. The symmetric supercapacitor (two-electrode system) was simply fabricated by using the prepared ZFO/rGO hybrid electrodes with the same mass of active materials as positive electrode and negative electrode. The electrochemical impedance spectroscopy (EIS) was measured at open circuit potential with an amplitude of 5 mV in the frequency range of 100 kHz to 100 mHz. The specific capacitance of the electrode material was calculated from the galvanic discharge curves using the formula $C = \Delta t / \Delta V m$, where C is the specific capacitance (F g^{-1}), I is the current (A), Δt is the discharge time (s), m is the mass of the active electrode material (g), and ΔV is the operating potential window (V) during the discharge. The mass loadings of electroactive materials on one current collector (nickel foam) are ca. 2 mg cm^{-2} .

3. Results and discussion Discussion

The ZFO/rGO hybrid fabrication with or without PEG-4000 is schematically illustrated in Fig. 1. It is noteworthy that a smaller ZFO nanoparticles is observed in the ZFO/rGO hybrid with use of PEG-4000 compared to the ZFO/rGO hybrid without use of PEG-4000 (L-ZFO/rGO). By controlling the size of ZFO nanoparticles with a smaller size, improved performance can be achieved. The smaller ZFO nanoparticles in the ZFO/rGO hybrid offer large specific surface area for easy access of electrolyte, shortened ion diffusion pathways for facilitated ion transport, and effective sites for redox reactions, making it possible to fully utilize the charge storage ability of ZFO. This is advantageous to L-ZFO/rGO with a large ZFO nanoparticles size in which only a fraction of the ZFO nanoparticles can contribute to charge storage.

The ZFO/rGO hybrid were first analyzed by scanning electron microscopy (SEM). Fig. 2a shows a typical SEM image of ZFO/rGO

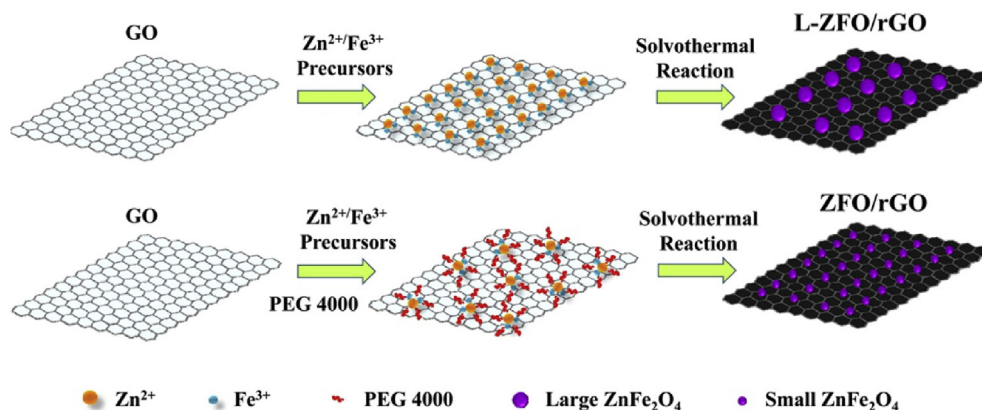


Fig. 1. Schematic illustration of the preparing procedure for ZFO/rGO hybrid with or without PEG-4000.

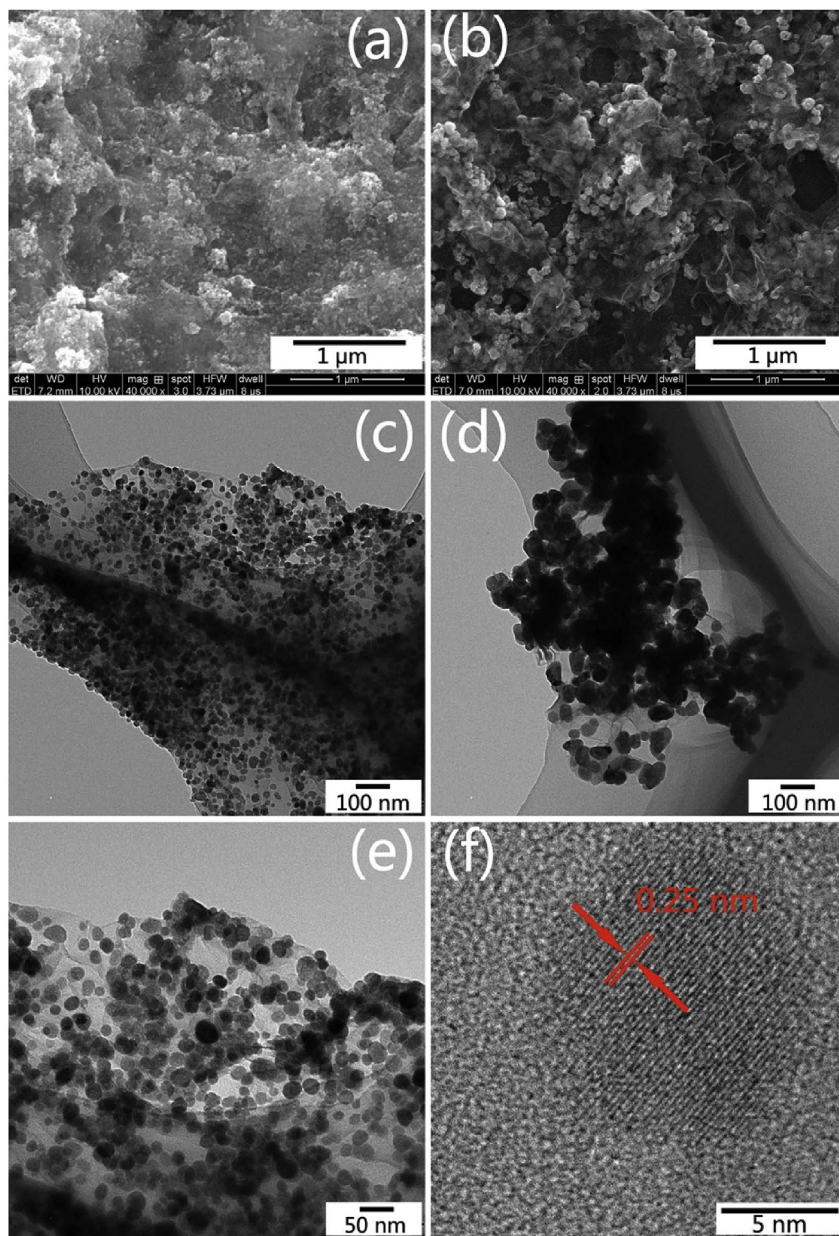


Fig. 2. SEM images of ZFO/rGO (a) and L-ZFO/rGO (b), TEM images of ZFO/rGO (c) and L-ZFO/rGO (d), enlarged TEM image of ZFO/rGO (e), and HRTEM image of ZFO/rGO (f).

hybrid, in which ZFO nanoparticles are homogeneously dispersed on the graphene surfaces. The rGO sheets are rough and wrinkled, which enables good mechanical strength, high electrical conductivity, and large surface area for ZFO/rGO hybrid. However, it clearly shows that most of the ZFO particles with larger size are deposited on the graphene sheets for L-ZFO/rGO (Fig. 2b). It can be deduced that the PEG-4000 played a critical role during the formation of ZFO particles on graphene sheets. The TEM images (Fig. 2c and d) further display a uniform coverage of the rGO sheets by ZFO particles without any obvious agglomeration. The ZFO average diameter is ~15 nm in ZFO/rGO hybrid, when it is ~60 nm in L-ZFO/rGO, as described by TEM images (Fig. 2c, d, e). Fig. 2f is the high resolution TEM (HRTEM) of ZFO particles, which shows the interplanar spacing between lattice fringes is 0.25 nm, corresponding to the (311) plane of the ZFO. The integration of the smaller ZFO particles on conductive rGO sheets provides better architecture for accessibility to the electrolyte ions from both sides of the rGO sheets and

for the rapid charge transport throughout the ZFO/rGO hybrid for high-energy storage.

Fig. 3 shows the X-ray diffraction (XRD) pattern of the ZFO/rGO and L-ZFO/rGO hybrid. All peaks can be indexed to the ZFO (JCPDS No. 22–1012), which confirms the formation of ZFO on rGO sheets. In addition, no obvious peak was observed at 25° , which suggests that highly disordered and few-layer rGO sheets are well-distributed in the ZFO/rGO hybrid, consistent with the previous reports [24,25]. The average crystallite sizes were calculated to be ca. 15 nm using the Scherer equation based on the (311) diffraction peak, suggesting that these nanoparticles are single-crystal structure [24]. Furthermore, the Raman spectrum is another essential tool to characterize the ZFO/rGO hybrid. As shown in Fig. 3, two prominent peaks at ~ 1335 and ~ 1597 cm^{-1} are derived from rGO, while the other peaks located at 212, 278, 392, 478, and 590 cm^{-1} are resulted from ZFO. This results confirm the formation of the ZFO/rGO hybrid. Moreover, the peaks of the ZFO/rGO hybrid have

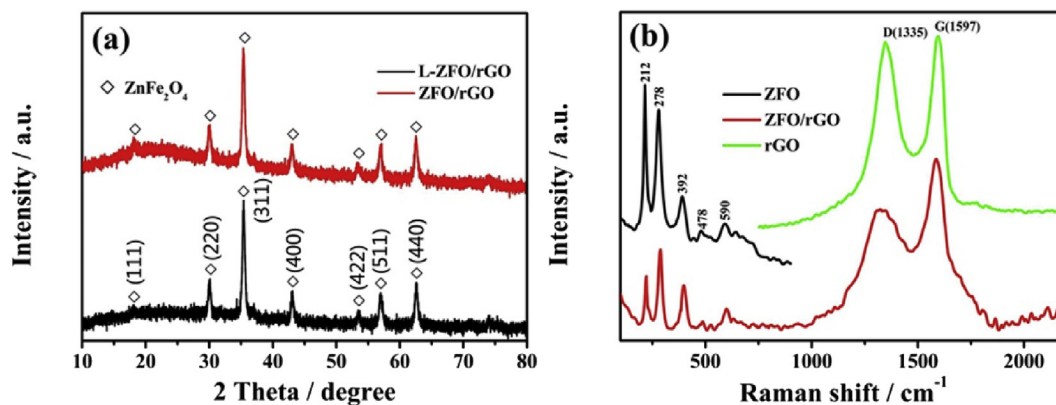


Fig. 3. (a) XRD patterns of the ZFO/rGO and L-ZFO/rGO; (b) Raman spectra of ZFO/rGO, rGO, and ZFO.

some shift and broadening compared with rGO and ZFO, revealing the electronic interactions between rGO and ZFO, which will facilitate electron transport between rGO and ZFO and thus enhance the rate capability [14,26,27].

The electrochemical properties of the ZFO/rGO hybrid electrode were firstly evaluated by cyclic voltammetry (CV) measurements with a standard three electrode system containing 2 M KOH electrolyte. The CV shape changes a little as the scan rate increases from 5 to 100 mV s^{-1} , and rapid current response upon voltage reversal occurs at each end potential for all the scan rates (Fig. 4a), indicating the good electrochemical capacitive properties of the ZFO/rGO hybrid electrodes. The galvanostatic charge–discharge (GCD) curves of the ZFO/rGO hybrid electrode at different current densities show triangular-shape, and the charge and the corresponding discharge curves are symmetric to each other (Fig. 4b), suggesting a rapid current–voltage response and good electrochemical reversibility. The specific capacitance is calculated from the discharge curve. The ZFO/rGO hybrid electrode exhibits a specific capacitance of 352.9, 327.6, 315.0, 304.2, 296.2, and 270 F g^{-1} at current densities of 1, 2, 3, 4, 5, and 10 A g^{-1} , respectively, which is higher or comparable to other ZFO based electrodes reported previously (Table S3).

For comparison, the CV and GCD measurements of L-ZFO/rGO were performed. Fig. 4c shows the CV curves of both ZFO/rGO and L-ZFO/rGO at a scan rate of 10 mV s^{-1} . The CV curve of ZFO/rGO show a much larger area indicating higher levels of stored charge compared to L-ZFO/rGO [28]. Fig. 4d shows the comparison of GCD curves for ZFO/rGO and L-ZFO/rGO at a constant current density of 1 A/g . The longer discharging time of ZFO/rGO represents the higher capacitance than that of L-ZFO/rGO. Owing to the improved electrode/electrolyte accessibility by virtue of the smaller ZFO size, the ZFO/rGO shows a significant increase in its capacitive behavior compared to the L-ZFO/rGO [25,29]. Variations of specific capacitance with increase of current density for ZFO/rGO and L-ZFO/rGO are shown in Fig. 4e. At lower current densities, electrolyte ions can fully penetrate into the electrode material, but at higher current densities, an effective utilization of the material is limited only to the outer surface of electrodes. Therefore, there is still around 76.5% initial capacitance retention even when the current density increases as high as 10 A/g for ZFO/rGO compared to the L-ZFO/rGO (64.7%), suggesting the good high-rate capability. The architecture of ZFO/rGO facilitate the rapid transport of the electrolyte ions and increase the electrochemical utilization of ZFO due to the smaller size. The cycling stability for ZFO/rGO and L-ZFO/rGO at a constant current density of 1 A/g are illustrated in Fig. 4f. The capacitance retention of both ZFO/rGO and L-ZFO/rGO obviously decreases at the beginning of the cyclic test, which is mainly attributed to the

irreversibility of Faradaic reactions or degradation at microstructural level [13]. However, it is found that 92.3% of the initial capacitance is retained for the ZFO/rGO electrode, whereas the L-ZFO/rGO electrode retained ~85.5% of the initial capacitance after 10000 cycles. The GCD curves of the ZFO/rGO hybrid electrode after 10000 cycles show the similar shape to the initial GCD curves of the ZFO/rGO hybrid electrode, further confirming satisfactory cycling stability (Fig. S2). The better stability of ZFO/rGO can be attributed to synergetic effect of high conductivity of rGO and well-dispersed small ZFO nanoparticles.

The relationship between the ZFO mass ratio and the electrochemical properties is also examined. The content of ZFO particles in the hybrid was controlled by varying the zinc and ferric salt concentration. The weight percentage of ZFO in the hybrid is determined by thermogravimetric analysis (TGA) as shown in Fig. 5a. The experiments were performed until 900 $^{\circ}\text{C}$ at a heating rate of 10 $^{\circ}\text{C min}^{-1}$ in air. Under this condition, the rGO sheets were burned up while ZFO was left. Accordingly, the mass ratio of ZFO in the ZFO/rGO hybrid can be estimated. The ratios of the ZFO to the rGO were gradually increased with the increasing zinc and ferric salt concentration (Fig. 5b). The GCD curves of the ZFO/rGO hybrid electrode at a current density of 1 A g^{-1} with different ZFO mass ratio are illustrated in Fig. 5c. With the increase of ZFO mass ratio, the capacitance initially increases and then reduces after reaching a maximal value, as shown in Fig. 5d. Generally, the decrease of the specific capacitance for ZFO/rGO hybrid is due to the dense packing of the ZFO nanoparticles, which resulted in a reduction of the conductivity and electrochemically activity. But, it is noteworthy that the largest capacitance is observed, when the ZFO mass ratio is as high as 82.3%, which is higher than previous results (under ~70% of ZFO/graphene hybrid [23,30]). It is well know that high mass ratio of pseudocapacitive materials in their carbon based hybrid can improve the specific capacitance of the composite electrode [31,32]. For L-ZFO/rGO, the ratios of the ZFO to the rGO have no obvious change with the increasing zinc and ferric salt concentration (Table S2 and Fig. S3). It has been proved that PEG-4000 plays important roles in controlling the size as well as the loading mass of ZFO in ZFO/rGO.

To testify the potential application of ZFO/rGO in supercapacitors, a symmetric supercapacitor was fabricated by using two identical ZFO/rGO electrodes and was tested at a potential range of 0–1.2 V in 2 M KOH electrolyte. Fig. 6a shows the CV curves of the symmetric supercapacitor based on ZFO/rGO at different scan rates. The rectangular-like shapes without distinct redox peaks demonstrated an ideal capacitive behavior. Furthermore, the CV profiles still retain a nearly rectangular shape without obvious change when the scan rate increased from 5 to 100 mV s^{-1} , suggesting

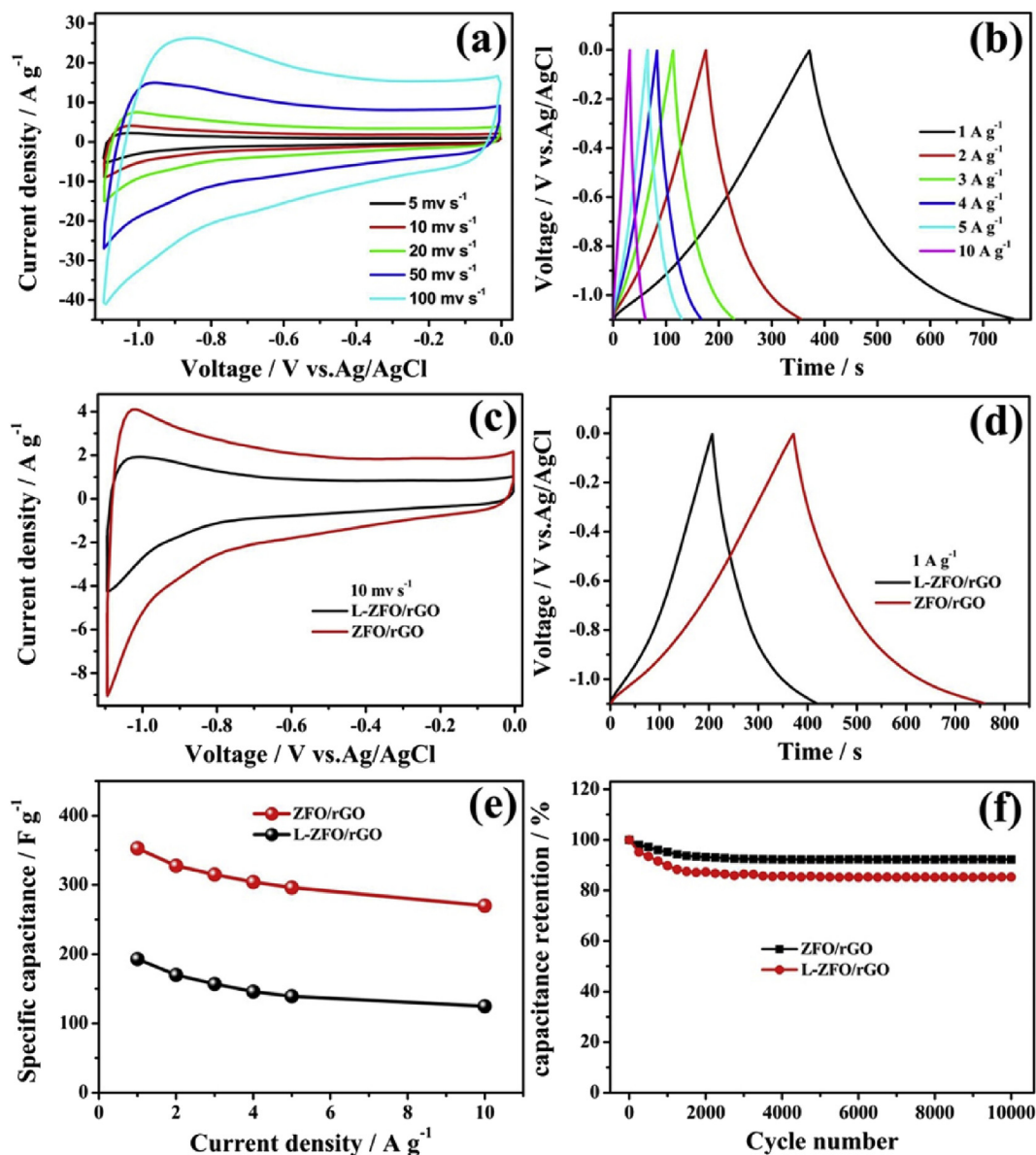


Fig. 4. (a) CV curves of the ZFO/rGO at different scan rates, (b) GCD curves of the ZFO/rGO at different current densities, (c) CV curves for the ZFO/rGO and L-ZFO/rGO electrodes at a scan rate of 10 mV/s, (d) GCD curves for the ZFO/rGO and L-ZFO/rGO electrodes at 1 A/g, (e) Variation of specific capacitance against different current density for the ZFO/rGO and L-ZFO/rGO, (f) the cycle life of the ZFO/rGO and L-ZFO/rGO electrodes at a current density of 1 A g⁻¹.

fast electron/ions transport in ZFO/rGO supercapacitor. Fig. 6b shows the galvanostatic charge/discharge (GCD) curves at various current densities. The triangular shaped galvanostatic charge/discharge curves once again manifest the good capacitive behavior. Fig. 6c displays the specific capacitance at different current densities calculated from discharge curves [27]. The maximum specific capacitance for the ZFO/rGO symmetric supercapacitor reaches 33.6 F g⁻¹ at 0.5 A g⁻¹. When the current density increased to 3 A g⁻¹, this device still retained about 78.3% initial specific capacitance, showing good rate capability of this device. The Ragone plot of ZFO/rGO supercapacitor is shown in Fig. 6d. The energy density can reach 6.7 Wh kg⁻¹ at a power density of 300 W kg⁻¹. It should be noted that the energy density was calculated under a low voltage of 1.2 V in a 2 M KOH aqueous electrolyte, which is still high and higher than that of commercial supercapacitor (~5 Wh/kg) [33–35]. The improved electrochemical performance for the ZFO/rGO electrode can be attributed to several factors: a shorten ion

transport distance due to the small ZFO nanoparticles (~15 nm), high ZFO loading mass (82.3%), and superior electrical conductivity of rGO. Such high ZFO loading mass (82.3%), large ion-accessible surface area (242.3 m²/g, Fig. S4), and fast electron/ions transport are very desirable for electrodes in high-specific and high-rate performance supercapacitors.

4. Conclusions

In summary, ZFO/rGO hybrid with a high ZFO mass ratio (82.3%) and a controllable ZFO particle size is systematically prepared. The structure of the resulting ZFO/rGO hybrid electrode demonstrates an efficient way to get high electrochemical performance. This unique structure combines the advantages of small ZFO nanoparticles (~15 nm), exceptional conductivity of rGO, and high ZFO loading mass (82.3%), leading to effective utilization of ZFO, fast ion/electron transport, and increased specific capacitance of the ZFO/

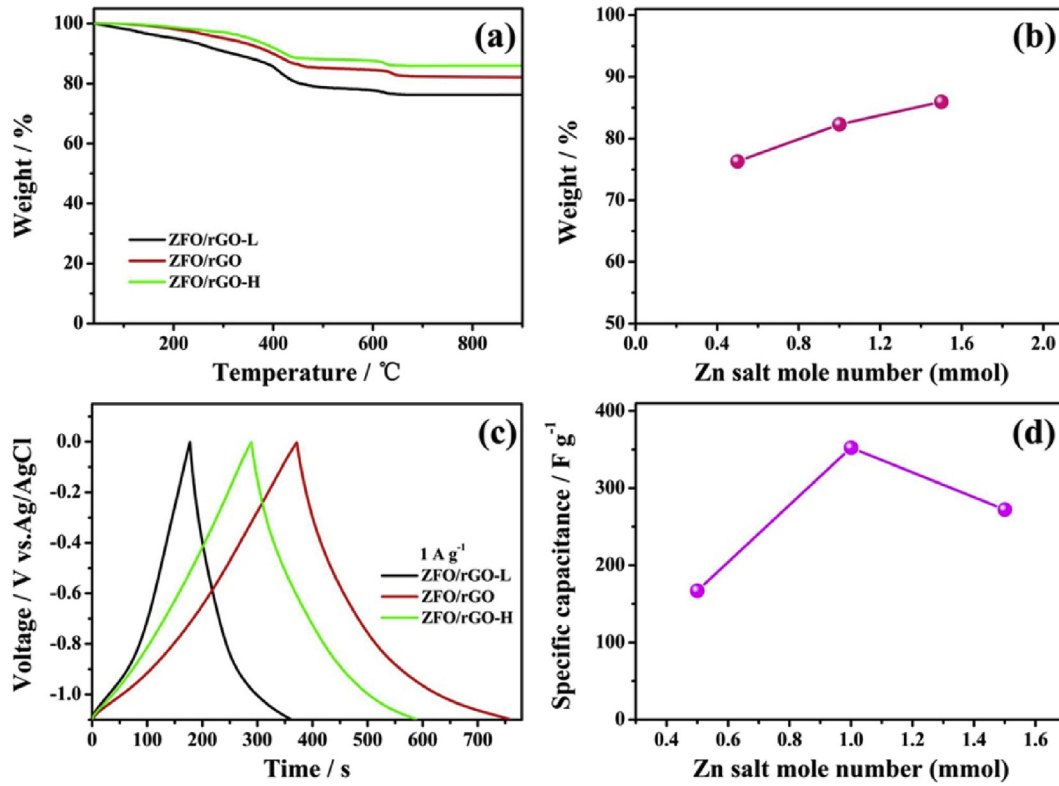


Fig. 5. (a) TGA curves of ZFO/rGO-L, ZFO/rGO, ZFO/rGO-H, (b) Mass ratio of ZFO in ZFO/rGO-L, ZFO/rGO, ZFO/rGO-H, (c) GCD curves for ZFO/rGO-L, ZFO/rGO, ZFO/rGO-H electrodes at 1 A/g, (d) Specific capacitance of ZFO/rGO-L, ZFO/rGO, ZFO/rGO-H electrodes at 1 A/g.

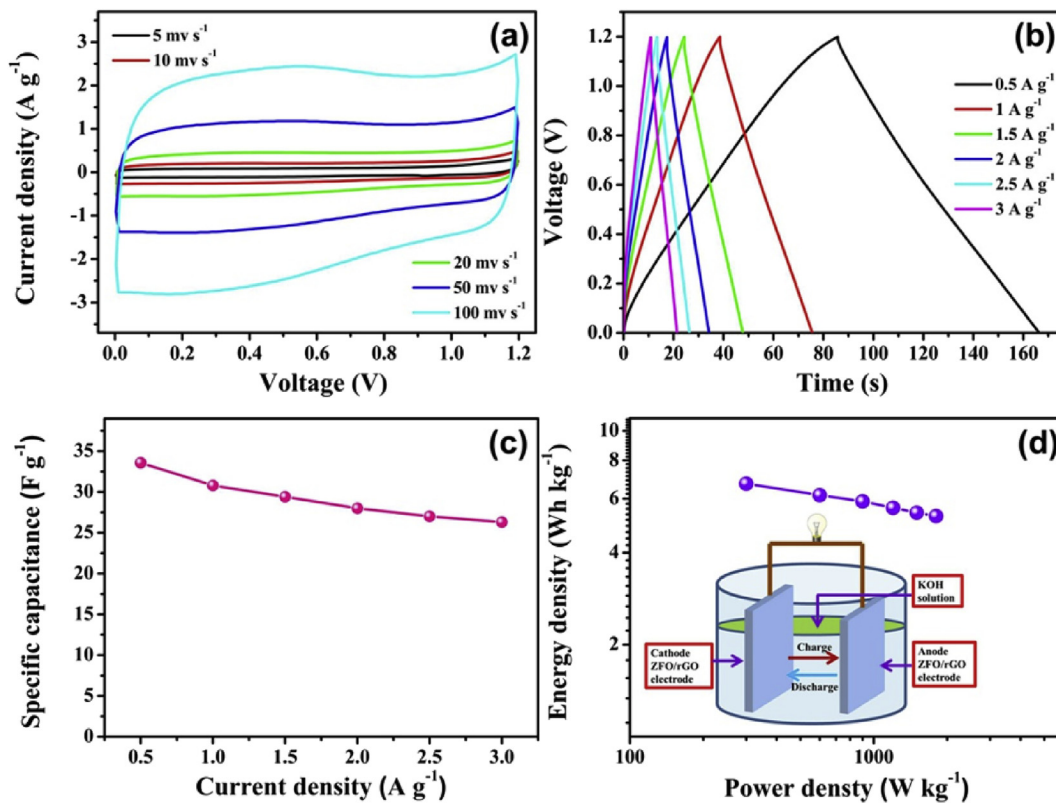


Fig. 6. (a) CV curves of symmetric supercapacitor based on ZFO/rGO, (b) GCD curves of symmetric supercapacitor based on ZFO/rGO, (c) Variation of specific capacitance against different current density for symmetric supercapacitor based on ZFO/rGO, (d) Ragone plot of symmetric supercapacitor based on ZFO/rGO.

rGO hybrid electrode. It delivered an enhanced specific capacitance and exhibited good rate performance as well as high cyclic stability. The specific capacitance of this hybrid achieve 352.9 F g^{-1} at current densities of 1 A g^{-1} , which is higher or comparable to other ZFO based electrodes. It also exhibits remarkable cyclic stability (92.3% retention after 10000 cycles) and good rate performance. The ZFO/rGO supercapacitor can reach high energy density (6.7 Wh kg^{-1}) within a low voltage of 1.2 V in a 2 M KOH aqueous electrolyte.

Acknowledgments

This work is supported by NSFC (51702123, 51472110), Shandong Provincial Natural Science Foundation (ZR2016EMB05, ZR2017ZB0315), University of Jinan Science Foundation (No. XKY1630). S.Y. thanks the start-up research funding and B.C. thanks the Taishan Scholar Professorship both from University of Jinan.

Appendix A. Supplementary data

Supplementary data related to this article can be found at <https://doi.org/10.1016/j.electacta.2018.02.028>.

References

- [1] R. Wang, P. Liu, J. Lang, L. Zhang, X. Yan, *Energy Storage Materials* 6 (2017) 53–60.
- [2] J. Lang, X. Zhang, B. Liu, R. Wang, J. Chen, X. Yan, *J. Energy Chem* 27 (2018) 43–56.
- [3] J. Sun, C. Wu, X. Sun, H. Hu, C. Zhi, L. Hou, C. Yuan, *J. Mater. Chem.* 5 (2017) 9443–9464.
- [4] C. Zhong, Y. Deng, W. Hu, J. Qiao, L. Zhang, J. Zhang, *Chem. Soc. Rev.* 44 (2015) 7484–7539.
- [5] H. Lu, X.S. Zhao, *Sustainable Energy & Fuels* 1 (2017) 1265–1281.
- [6] L. Zhang, S.X. Dou, H.K. Liu, Y. Huang, X. Hu, *Advanced Science* 3 (2016) 1600115–1600123.
- [7] R. Kumar, E. Joanni, R.K. Singh, E.T.S.G. da Silva, R. Savu, L.T. Kubota, S.A. Moshkalev, *J. Colloid Interface Sci.* 507 (2017) 271–278.
- [8] R.K. Singh, R. Kumar, D.P. Singh, *RSC Adv.* 6 (2016) 64993–65011.
- [9] F. Wang, X. Wu, X. Yuan, Z. Liu, Y. Zhang, L. Fu, Y. Zhu, Q. Zhou, Y. Wu, W. Huang, *Chem. Soc. Rev.* 46 (2017) 6816–6854.
- [10] S. Zhang, C. Li, X. Zhang, X. Sun, K. Wang, Y. Ma, *ACS Appl. Mater. Interfaces* 9 (2017) 17136–17144.
- [11] R. Kumar, R.K. Singh, P.K. Dubey, D.P. Singh, R.M. Yadav, *ACS Appl. Mater. Interfaces* 7 (2015) 15042–15051.
- [12] R. Kumar, R.K. Singh, A.R. Vaz, R. Savu, S.A. Moshkalev, *ACS Appl. Mater. Interfaces* 9 (2017) 8880–8890.
- [13] R. Kumar, R.K. Singh, P.K. Dubey, D.P. Singh, R.M. Yadav, R.S. Tiwari, *Adv. Mater. Interfaces* 2 (2015) 1500191–1500203.
- [14] R. Kumar, H.-J. Kim, S. Park, A. Srivastava, I.-K. Oh, *Carbon* 79 (2014) 192–202.
- [15] R. Kumar, R.K. Singh, P. Kumar Dubey, D.P. Singh, R.M. Yadav, R.S. Tiwari, *RSC Adv.* 5 (2015) 7112–7120.
- [16] R. Kumar, R.K. Singh, R. Savu, P.K. Dubey, P. Kumar, S.A. Moshkalev, *RSC Adv.* 6 (2016) 26612–26620.
- [17] M.M. Vadiyar, S.S. Kolekar, J.-Y. Chang, Z. Ye, A.V. Ghule, *ACS Appl. Mater. Interfaces* 9 (2017) 26016–26028.
- [18] Z.-Y. Yu, L.-F. Chen, S.-H. Yu, *J. Mater. Chem.* 2 (2014) 10889–10894.
- [19] M. Zhu, D. Meng, C. Wang, G. Diao, *ACS Appl. Mater. Interfaces* 5 (2013) 6030–6037.
- [20] A. Sutka, N. Doebelin, *J. Jpn. Soc. Powder Powder Metallurgy* 61 (2014) S81–S84.
- [21] L. Hou, L. Lian, L. Zhang, G. Pang, C. Yuan, X. Zhang, *Adv. Funct. Mater.* 25 (2015) 238–246.
- [22] M.M. Vadiyar, S.S. Kolekar, N.G. Deshpande, J.-Y. Chang, A.A. Kashale, A.V. Ghule, *Ionics* 23 (2017) 741–749.
- [23] L. Li, H. Bi, S. Gai, F. He, P. Gao, Y. Dai, X. Zhang, D. Yang, M. Zhang, P. Yang, *Sci. Rep.* 7 (2017) 43116.
- [24] S. Yang, X. Song, P. Zhang, J. Sun, L. Gao, *Small* 10 (2014) 2270–2279.
- [25] S. Yang, X. Song, P. Zhang, L. Gao, *J. Mater. Chem.* 1 (2013) 14162–14169.
- [26] S. Yang, Y. Lin, X. Song, P. Zhang, L. Gao, *ACS Appl. Mater. Interfaces* 7 (2015) 17884–17892.
- [27] S. Yang, X. Song, P. Zhang, L. Gao, *J. Mater. Chem.* 3 (2015) 6136–6145.
- [28] S. Yang, X. Song, P. Zhang, L. Gao, *ACS Appl. Mater. Interfaces* 5 (2013) 3317–3322.
- [29] R. Wang, J. Lang, Y. Liu, Z. Lin, X. Yan, *NPG Asia Mater.* 7 (2015) e183.
- [30] L. Lin, Q. Pan, *J. Mater. Chem.* 3 (2015) 1724–1729.
- [31] G. Sun, L. Ma, J. Ran, X. Shen, H. Tong, *J. Mater. Chem.* 4 (2016) 9542–9554.
- [32] L. Ji, P. Meduri, V. Agubra, X. Xiao, M. Alcoutlabi, *Adv. Energy Mater* 6 (2016) 1502159–1502231.
- [33] J. Huang, J. Wang, C. Wang, H. Zhang, C. Lu, J. Wang, *Chem. Mater.* 27 (2015) 2107–2113.
- [34] F. Béguin, V. Presser, A. Balducci, E. Frackowiak, *Adv. Mater* 26 (2014) 2219–2251.
- [35] Z. Wen, X. Wang, S. Mao, Z. Bo, H. Kim, S. Cui, G. Lu, X. Feng, J. Chen, *Adv. Mater* 24 (2012) 5610–5616.